Computers & Fluids 44 (2011) 178–186

Contents lists available at ScienceDirect

Computers & Fluids

journal homepage: www.elsevier.com/locate/compfluid

Accurate contact angle boundary conditions for the Cahn–Hilliard equations

Hyun Geun Lee, Junseok Kim *

Department of Mathematics, Korea University, Seoul 136-701, Republic of Korea

ARTICLE INFO

Article history:
Received 8 February 2010
Received in revised form 2 September 2010
Accepted 24 December 2010
Available online 8 January 2011

Keywords:
Cahn–Hilliard equation
Contact angle
Unconditionally gradient stable scheme
Nonlinear multigrid method

ABSTRACT

The contact angle dynamics between a two-phase interface and a solid surface is important in physical interpretations, mathematical modeling, and numerical treatments. We present a novel formulation based on a characteristic interpolation for the contact angle boundary conditions for the Cahn–Hilliard equation. The new scheme inherits characteristic properties, such as the mass conservation, the total energy decrease, and the unconditionally gradient stability. We demonstrate the accuracy and robustness of the proposed contact angle boundary formulation with various numerical experiments. The numerical results indicate a potential usefulness of the proposed method for accurately calculating contact angle problems.

1. Introduction

The contact angle is the dihedral angle formed at the interface among three fluid phases α, β, γ or between two fluid phases α, β and a solid surface γ, as shown in Fig. 1a and b. We shall represent the dihedral angles by θ_α, θ_β, and θ_γ, thus naming them after the phases they contain. At equilibrium, the net force on any element of the three phase lines vanishes. Resolving this force in directions that lie, respectively, along the $\alpha\beta$, $\beta\gamma$, and $\gamma\alpha$ interfaces and are perpendicular to the three phases line, we have

$$\begin{aligned}
&\sigma_{\alpha\beta} + \sigma_{\beta\gamma}\cos\theta_\beta + \sigma_{\gamma\alpha}\cos\theta_\alpha = 0,\\
&\sigma_{\alpha\beta}\cos\theta_\beta + \sigma_{\beta\gamma} + \sigma_{\gamma\alpha}\cos\theta_\gamma = 0,\\
&\sigma_{\alpha\beta}\cos\theta_\alpha + \sigma_{\beta\gamma}\cos\theta_\gamma + \sigma_{\gamma\alpha} = 0,
\end{aligned} \tag{1}$$

where $\sigma_{\alpha\beta}$ is the tension of the $\alpha\beta$ interface, etc. [1]. When the γ phase is a solid as shown in Fig. 1b, the angle θ_γ is π. In this case, the second equation of (1) becomes

$$\sigma_{\alpha\beta}\cos\theta_\beta = \sigma_{\gamma\alpha} - \sigma_{\beta\gamma},$$

which is Young's equation [2] and we denote this θ_β by θ.

Modeling and numerical representations of the contact line between a two-phase interface and a solid surface are still open problems from the physical, mathematical, and numerical points of view [3]. In this paper, we consider an accurate and robust numerical scheme for the Cahn–Hilliard (CH) equation with contact angle boundary conditions. The quantity $c(\mathbf{x},t)$ is defined to be the difference between the concentrations of the two mixtures (e.g., $c(\mathbf{x},t) = (m_\alpha - m_\beta)/(m_\alpha + m_\beta)$ where m_α and m_β are the masses of phases α and β). The Cahn–Hilliard equation is given by

$$\frac{\partial c(\mathbf{x},t)}{\partial t} = M\Delta\mu(\mathbf{x},t), \quad \mathbf{x}\in\Omega, \quad 0 < t \leqslant T, \tag{2}$$

$$\mu(\mathbf{x},t) = F'(c(\mathbf{x},t)) - \epsilon^2\Delta c(\mathbf{x},t), \tag{3}$$

$$\frac{\partial c(\mathbf{x},t)}{\partial \mathbf{n}} = -\frac{f_w'(c(\mathbf{x},t))}{\epsilon^2}, \quad \mathbf{x}\in\partial\Omega, \quad 0 < t \leqslant T, \tag{4}$$

$$\frac{\partial \mu(\mathbf{x},t)}{\partial \mathbf{n}} = 0, \tag{5}$$

where $\Omega \subset \mathbf{R}^2$ and $\mathbf{n}$ is the direction normal to and into the wall. This equation was introduced to model spinodal decomposition and coarsening phenomena in binary alloys [4,5]. It arises from the total Helmholz free energy functional

$$\mathscr{F}(c) = \mathscr{E}(c) + \mathscr{W}(c) = \int_\Omega \left(F(c) + \frac{\epsilon^2}{2}|\nabla c|^2\right)d\mathbf{x} + \int_{\partial\Omega} f_w(c)ds,$$

where $F(c) = 0.25(c^2-1)^2$ is the Helmholz free energy (Fig. 2a) of a unit volume of homogeneous material of composition c and ϵ is a positive constant. $f_w(c) = \epsilon(c^3 - 3c)/(3\sqrt{2})\cos\theta$ is the specific wall free energy, which depends only on the concentration at the solid surface and the contact angle θ. The surface integral term $\mathscr{W}(c)$ represents the contribution of solid-fluid interactions. Fig. 2b shows $f_w(c)$ with $\epsilon = 0.01$ and $\theta = 45°$, 60°, 90°, and 135°.

Next, we derive the governing Eqs. (2)–(5). To derive the variation of the functional $\mathscr{F}$, with $\int_\Omega \phi d\mathbf{x} = 0$, we calculate the following

* Corresponding author.
E-mail address: cfdkim@korea.ac.kr (J. Kim).
URL: http://math.korea.ac.kr/~cfdkim/ (J. Kim).

0045-7930/$ - see front matter © 2011 Elsevier Ltd. All rights reserved.
doi:10.1016/j.compfluid.2010.12.031

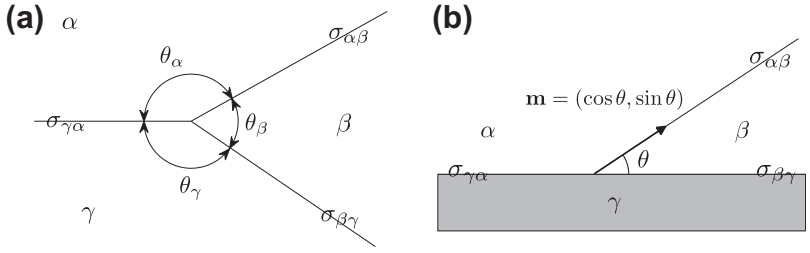

Fig. 1. Definitions of dihedral angles at the junctions of three surfaces where three phases meet. (a) α, β, and γ are fluids. (b) α and β are fluids, γ is a solid.

$$\begin{aligned}\frac{d}{d\eta}\mathscr{F}(c+\eta\phi)\Big|_{\eta=0} &= \int_\Omega \left(\phi F'(c) + \epsilon^2 \nabla\phi\cdot\nabla c\right) d\mathbf{x} + \int_{\partial\Omega} \phi f_w'(c) ds \\ &= \int_\Omega \left(F'(c) - \epsilon^2\Delta c\right)\phi\, d\mathbf{x} \\ &\quad + \int_{\partial\Omega}\left(\epsilon^2\frac{\partial c}{\partial \mathbf{n}} + f_w'(c)\right)\phi\, ds \\ &= \int_\Omega \left(F'(c) - \epsilon^2\Delta c\right)\phi\, d\mathbf{x},\end{aligned}$$

where we have used a natural boundary condition,

$$\frac{\partial c}{\partial \mathbf{n}} = -\frac{f_w'(c)}{\epsilon^2} = \frac{1-c^2}{\sqrt{2}\epsilon}\cos\theta. \tag{6}$$

This boundary condition becomes Eq. (4) and has been widely used for the contact angle boundary conditions [6–13]. However, Eq. (6) is not easy to implement accurately since we need to evaluate its value at the boundary and we do not know the concentration value at the boundary.

Now we get the chemical potential μ as the variational derivative of $\mathscr{F}$ with respect to c

$$\mu := \frac{\delta\mathscr{F}}{\delta c} = F'(c) - \epsilon^2\Delta c$$

and we define the flux, $\mathscr{J} := -M\nabla\mu$, where $M > 0$ is a diffusional mobility. As a consequence of mass conservation, we have $c_t = -\nabla\cdot\mathscr{J}$, which gives us the CH Eqs. (2) and (3). The mass conserving boundary condition is

$$\frac{\partial\mu}{\partial\mathbf{n}} = 0. \tag{7}$$

So that

$$\frac{d}{dt}\int_\Omega c\, d\mathbf{x} = \int_\Omega c_t\, d\mathbf{x} = M\int_\Omega \Delta\mu\, d\mathbf{x} = -M\int_{\partial\Omega}\frac{\partial\mu}{\partial\mathbf{n}}\, ds = 0. \tag{8}$$

We differentiate the energy $\mathscr{F}$ with respect to time variable to get

$$\begin{aligned}\frac{d}{dt}\mathscr{F}(t) &= \int_\Omega (F'(c)c_t + \epsilon^2\nabla c\cdot\nabla c_t) d\mathbf{x} + \int_{\partial\Omega} f_w'(c)c_t\, ds \\ &= \int_\Omega \mu c_t\, d\mathbf{x} + \int_{\partial\Omega}\left(\epsilon^2\frac{\partial c}{\partial\mathbf{n}} + f_w'(c)\right)c_t\, ds = \int_\Omega \mu M\Delta\mu\, d\mathbf{x} \\ &= \int_{\partial\Omega}\mu M\frac{\partial\mu}{\partial\mathbf{n}}\, ds - \int_\Omega M\nabla\mu\cdot\nabla\mu\, d\mathbf{x} = -\int_\Omega M|\nabla\mu|^2\, d\mathbf{x},\end{aligned} \tag{9}$$

which guarantees that the free energy functional decreases with time. Here we used the no-flux boundary condition (7).

The CH equation with Neumann [14,15], periodic [16] or dynamic [17] boundary conditions has been studied intensively with numerical methods. In recent work [18], the authors presented simulations of dynamic wetting far from equilibrium based on phase field theory. However, only a few authors studied the CH equation with contact angle boundary conditions [6,7]. We propose a new accurate and robust contact angle boundary condition that is based on a characteristic interpolation.

This paper is organized as follows. In Section 2, we describe the proposed contact angle boundary condition and its numerical algorithm. The numerical results that demonstrate the accuracy and robustness of the proposed contact angle boundary formulation are described in Section 3. A discussion is presented in Section 4.

2. Proposed contact angle boundary condition and numerical algorithm

In this section, we propose a method which gives an accurate contact angle boundary condition as well as a numerical stability. Our method is based on a technique for solving partial differential equations known as the method of characteristics. First, we present an unconditionally gradient stable scheme for the CH equation in two dimensional space $\Omega = (a,b)\times(c,d)$ [19–21]. Let N_x and N_y be

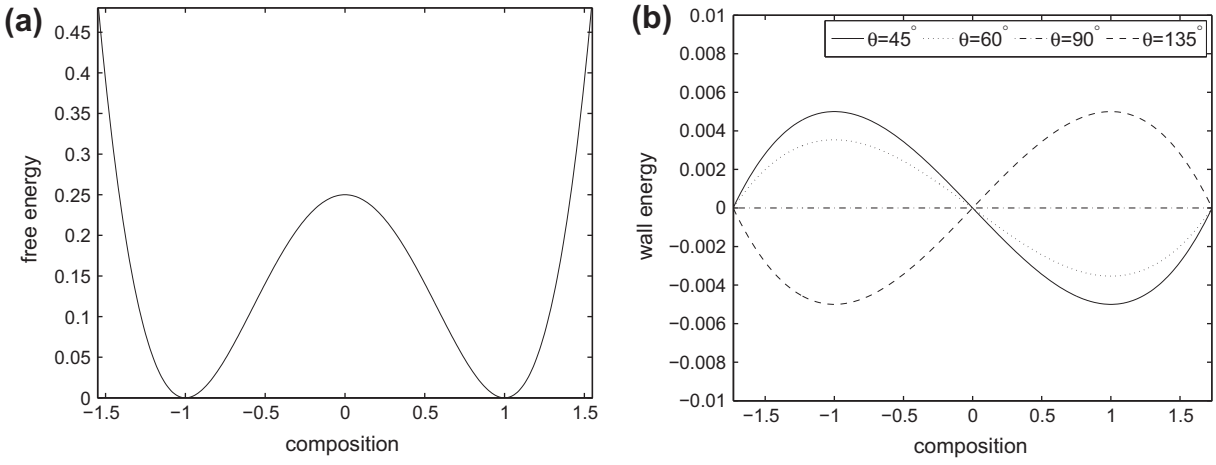

Fig. 2. (a) $F(c) = 0.25(c^2-1)^2$. (b) $f_w(c) = \epsilon(c^3-3c)/(3\sqrt{2})\cos\theta$ and $\epsilon = 0.01$.

positive even integers, $h = (b-a)/N_x$ be the uniform mesh size, $\Omega_h = \{(x_i, y_j): x_i = (i-0.5)h,\ y_j = (j-0.5)h,\ 1 \leqslant i \leqslant N_x,\ 1 \leqslant j \leqslant N_y\}$ be the set of cell-centers, and c_{ij}^n be an approximation of $c(x_i, y_j, n\Delta t)$, where $\Delta t = T/N_t$ is the time step, T is the final time, and N_t is the total number of time steps. We take $M \equiv 1$ for convenience. Then, an unconditionally gradient stable time and centered difference space discretization of Eqs. (2) and (3) is

$$\frac{c_{ij}^{n+1} - c_{ij}^n}{\Delta t} = \Delta_d v_{ij}^{n+1} - \Delta_d c_{ij}^n, \tag{10}$$

$$v_{ij}^{n+1} = F'(c_{ij}^{n+1}) + c_{ij}^{n+1} - \epsilon^2 \Delta_d c_{ij}^{n+1}. \tag{11}$$

The resulting nonlinear system of Eqs. (10) and (11) is solved efficiently using a nonlinear multigrid method. The method is described in [21] in detail. Now, we describe how we impose the contact angle boundary conditions (4) and (5). When the contact angle is $\theta = 90°$, an equilibrium solution to Eq. (2) in an infinite domain would be

$$c(x,y) = \tanh\frac{x}{\sqrt{2}\epsilon}. \tag{12}$$

We can consider x in the argument of the tanh() function as the signed distance from the line $x = 0$. Eq. (12) with $\epsilon = 0.01$ is shown in Fig. 3a on the domain $\Omega = (-4,4) \times (-1, 1)$. When the contact angle is $\theta = 45°$, an equilibrium state (see Fig. 3b) is given as

$$c(x,y) = \tanh\frac{x-y}{2\epsilon}. \tag{13}$$

In this case $(x-y)/\sqrt{2}$ is the signed distance from the line $x - y = 0$. When the contact angle is $\alpha = \tan^{-1}(0.5)\,(180/\pi)°$, we have

$$c(x,y) = \tanh\frac{\sin(\alpha)x - \cos(\alpha)y}{\sqrt{2}\epsilon}, \tag{14}$$

where $\sin(\alpha)x - \cos(\alpha)y$ is the signed distance from the line $\sin(\alpha)x - \cos(\alpha)y = 0$. This is shown in Fig. 3c. Fig. 3d shows contour plots of Eqs. (12)–(14) at the levels −0.9, −0.6, −0.3, 0, 0.3, 0.6, 0.9.

From these observations, data at the ghost points should be obtained from the characteristic line whose slope is $\tan\theta$.

Let the phase-field be defined as

$$c(x,y) = \tanh\frac{\sin(\theta)x - \cos(\theta)y}{\sqrt{2}\epsilon},$$

which means that the contact angle is θ at the origin. For a contact angle boundary condition, we have

$$\nabla c \cdot \mathbf{m} = 0,$$

where $\mathbf{m} = (\cos\theta, \sin\theta)$ is a unit tangent vector to the interface at the contact point and θ is a prescribed contact angle (see Fig. 1b). When the contact angle is $\theta = 90°$, we have

$$c_{i,0}^{n+1} = c_{i,1}^{n+1}.$$

When the contact angle is $\theta = 45°$, we have

$$c_{i,0}^{n+1} = \begin{cases} c_{i+1,1}^{n+1} & \text{if } c_{i-1,1}^{n+1} > c_{i+1,1}^{n+1}, \\ c_{i-1,1}^{n+1} & \text{otherwise.} \end{cases}$$

When the contact angle is $\theta = \tan^{-1}(0.5)(180/\pi)°$, we have

$$c_{i,0}^{n+1} = \begin{cases} c_{i+2,1}^{n+1} & \text{if } c_{i-1,1}^{n+1} > c_{i+1,1}^{n+1}, \\ c_{i-2,1}^{n+1} & \text{otherwise.} \end{cases}$$

These interpolations are shown in Fig. 4a. If the prescribed contact angle is not particular angles $(\theta = 90°, 45°, \frac{180}{\pi}\tan^{-1}(0.5)°)$, then we use an interpolation between the two closest points. For example, when $\theta = 60°$, the angle is between $\theta = 45°$ and $\theta = 90°$, therefore we use $c_{i,1}^{n+1}$ and $c_{i+1,1}^{n+1}$ to get $c_{i,0}^{n+1}$ value.

$$c_{i,0}^{n+1} = \begin{cases} \left(1 - \frac{1}{\sqrt{3}}\right)c_{i,1}^{n+1} + \frac{1}{\sqrt{3}}c_{i+1,1}^{n+1} & \text{if } c_{i-1,1}^{n+1} > c_{i+1,1}^{n+1}, \\ \frac{1}{\sqrt{3}}c_{i-1,1}^{n+1} + \left(1 - \frac{1}{\sqrt{3}}\right)c_{i,1}^{n+1} & \text{otherwise.} \end{cases}$$

This is shown in Fig. 4b. In general, when $\theta \neq 0°, 90°, 180°$, the characteristic line is $y = \tan(\theta)x$ and the interpolation position of

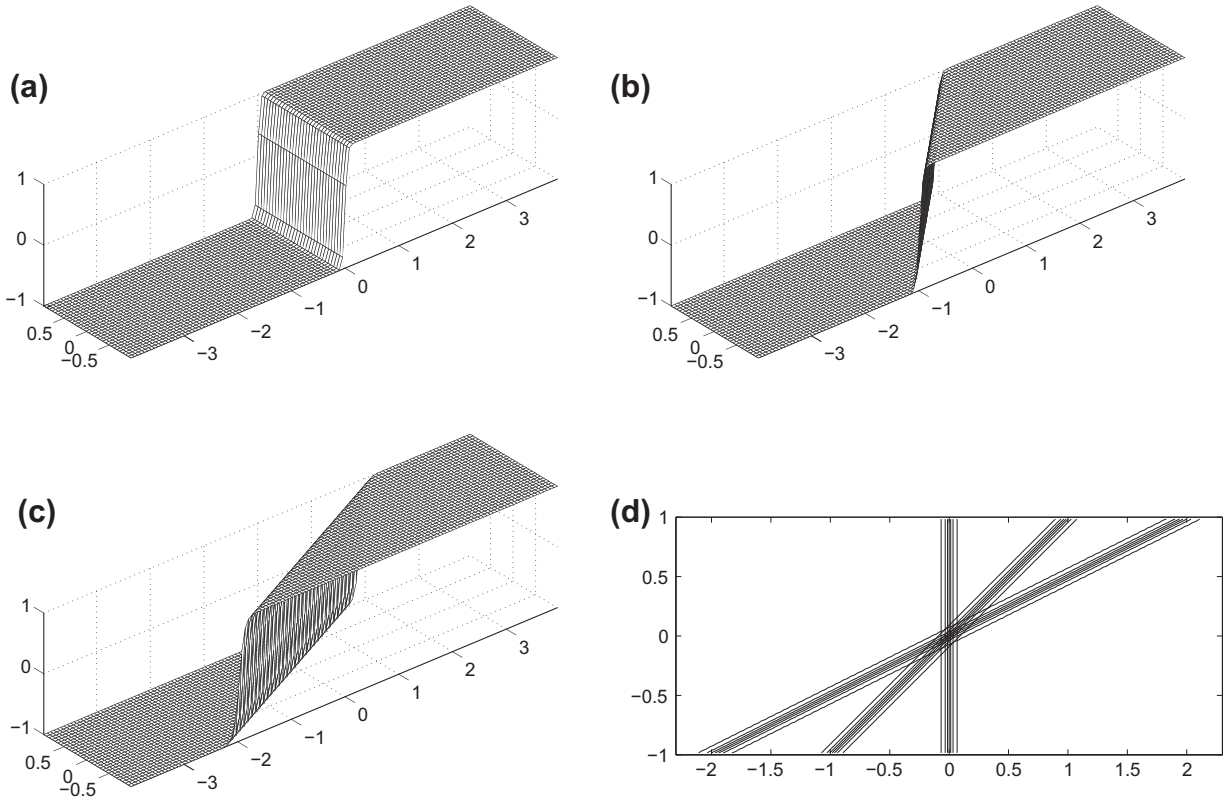

Fig. 3. (a) $c(x,y) = \tanh\frac{x}{\sqrt{2}\epsilon}$, (b) $c(x,y) = \tanh\frac{x-y}{2\epsilon}$, (c) $c(x,y) = \tanh\frac{\sin(\alpha)x-\cos(\alpha)y}{\sqrt{2}\epsilon}$, and (d) contour plots of $c(x,y)$ at −0.9, −0.6, −0.3, 0, 0.3, 0.6, 0.9 with $\epsilon = 0.01$.

x-coordinate is $x = h/\tan(\theta)$. We can write x as a sum of an integer part and a fraction part, i.e., $x = k + \alpha$, where k is an integer and $0 \leqslant \alpha < 1$. Then the characteristic interpolation is defined as

$$c_{i,0}^{n+1} = \begin{cases} (1-\alpha)c_{i+k,1}^{n+1} + \alpha c_{i+k+1,1}^{n+1} & \text{if } c_{i-1,1}^{n+1} > c_{i+1,1}^{n+1}, \\ \alpha c_{i+k-1,1}^{n+1} + (1-\alpha)c_{i+k,1}^{n+1} & \text{otherwise.} \end{cases}$$

Fig. 5 shows '$\circ$' and '$*$' are $c_{i,1}$ and $c_{i,0}$ values inside and outside of the bottom domain boundary, respectively. The contact angles are (a) $\theta = 90°$, (b) $\theta = 45°$, and (c) $\theta = \tan^{-1}(0.5)(180/\pi)°$. Line segments represent the difference, $|c_{i,1} - c_{i,0}|$. As we can see in Fig. 5, the difference $|c_{i,1} - c_{i,0}|$ for particular angles (except $\theta = 90°$) is not uniform. There is this difference in the transition region, however, there is no significant difference outside the region.

The core of the proposed algorithm is a characteristic interpolation, which gives both stability and accuracy. In order to get the mass conservation, we should get

$$\begin{aligned} 0 &= \sum_{i=1}^{N_x}\sum_{j=1}^{N_y} \frac{c_{ij}^{n+1} - c_{ij}^{n}}{\Delta t} = \sum_{i=1}^{N_x}\sum_{j=1}^{N_y} \Delta_d\left(v_{ij}^{n+1} - c_{ij}^{n}\right) \\ &= -\sum_{j=1}^{N_y} \frac{\left(v_{1j}^{n+1} - v_{0j}^{n+1}\right) - \left(c_{1j}^{n} - c_{0j}^{n}\right)}{h^2} \\ &\quad + \sum_{j=1}^{N_y} \frac{\left(v_{N_x+1,j}^{n+1} - v_{N_x,j}^{n+1}\right) - \left(c_{N_x+1,j}^{n} - c_{N_x,j}^{n}\right)}{h^2} \\ &\quad - \sum_{i=1}^{N_x} \frac{\left(v_{i,1}^{n+1} - v_{i,0}^{n+1}\right) - \left(c_{i,1}^{n} - c_{i,0}^{n}\right)}{h^2} \\ &\quad + \sum_{i=1}^{N_x} \frac{\left(v_{i,N_y+1}^{n+1} - v_{i,N_y}^{n+1}\right) - \left(c_{i,N_y+1}^{n} - c_{i,N_y}^{n}\right)}{h^2}. \end{aligned}$$

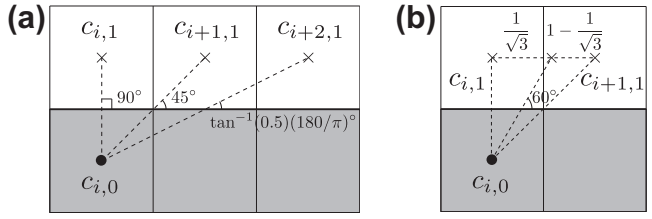

Fig. 4. (a) Illustration of the characteristic interpolation stencil for particular contact angles ($\theta = 90°$, $45°$, $\tan^{-1}(0.5)(180/\pi)°$) at a domain boundary. (b) Characteristic interpolation stencil for the contact angle $\theta = 60°$ at a domain boundary.

If we impose numerical no-flux boundary conditions, then we have mass conserving properties.

$$\begin{aligned} v_{0,j}^{n+1} &= v_{1,j}^{n+1} - c_{1,j}^{n} + c_{0,j}^{n}, \\ v_{N_x+1,j}^{n+1} &= v_{N_x,j}^{n+1} + c_{N_x+1,j}^{n} - c_{N_x,j}^{n} \text{ for} 1 \leqslant j \leqslant N_y, \\ v_{i,0}^{n+1} &= v_{i,1}^{n+1} - c_{i,1}^{n} + c_{i,0}^{n}, \\ v_{i,N_y+1}^{n+1} &= v_{i,N_y}^{n+1} + c_{i,N_y+1}^{n} - c_{i,N_y}^{n} \text{ for} 1 \leqslant i \leqslant N_x. \end{aligned}$$

This is the numerical boundary condition for Eq. (5). To solve the discrete system efficiently at the implicit time-level, we have used an unconditionally stable scheme with a nonlinear multigrid method. For a detailed description of the numerical method used in solving the discrete equations, refer to [22].

Recently, Ding and Spelt [6] proposed a new geometric formulation. We briefly review the geometric formulation. The normal vector to the interface can be written in terms of the gradient of c as $\mathbf{n}_s = \nabla c/|\nabla c|$. At the contact line, $\mathbf{n}_s$ intersects the solid substrate at an angle of θ, where θ is the contact angle (see Fig. 6a). Then, the contact angle can be computed geometrically in terms of c by

$$\tan\left(\frac{\pi}{2} - \theta\right) = \frac{\mathbf{n}\cdot\nabla c}{|\nabla c - (\mathbf{n}\cdot\nabla c)\mathbf{n}|}. \tag{15}$$

Eq. (15) is referred to as a geometric formulation for the computation of the contact angle θ. For example, to evaluate $c_{i,0}$ values, we use the following extrapolation.

$$c_{i,0} = c_{i,2} - \tan\left(\frac{\pi}{2} - \theta\right)|c_{i+1,1} - c_{i-1,1}|.$$

Note that to get the ghost cell value (circled x), we use three interior values (x). This extrapolation is effectively more accurate at the open circle than at the solid circle position at the domain boundary (Fig. 6b).

3. Numerical results

In this section, we perform numerical experiments such as equilibrium contact angles with a mesh refinement convergence test, advancing drop by contact angle difference, stability, and drop impact on a solid surface with/without the gravity effect in order to demonstrate the accuracy and robustness of the proposed contact angle boundary algorithm. In this experiment, for simplicity of presentation, we apply the periodic boundary condition in x-direction and zero Neumann boundary condition at the top of the domain. In the bottom of the domain, we prescribe a contact angle θ.

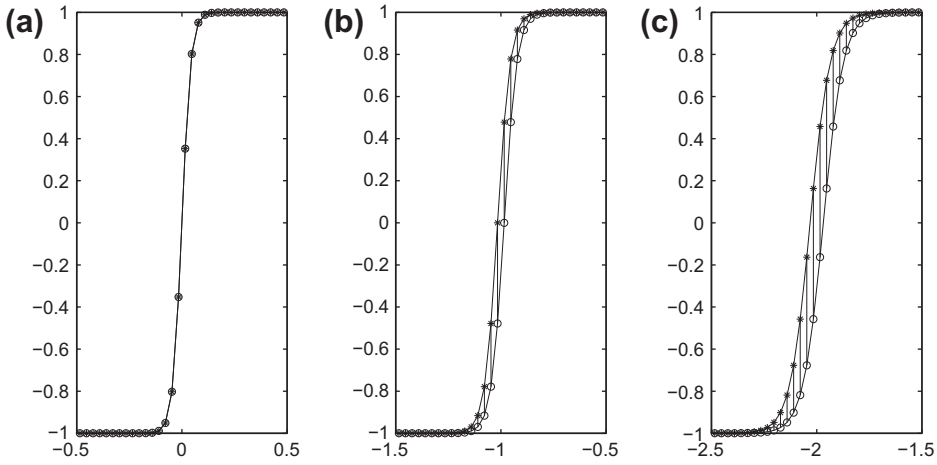

Fig. 5. '$\circ$' and '$*$' are $c_{i,1}$ and $c_{i,0}$ values inside and outside of the bottom domain boundary, respectively. (a) $\theta = 90°$, (b) $\theta = 45°$, and (c) $\theta = \tan^{-1}(0.5)(180/\pi)°$. Line segments represent the difference, $|c_{i,1} - c_{i,0}|$.

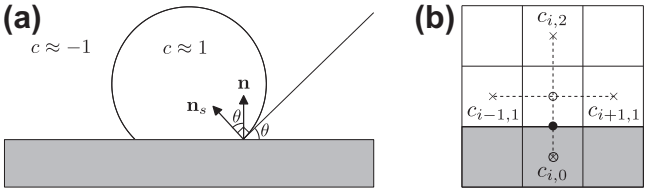

Fig. 6. (a) Contact angle θ, unit normal vector $\mathbf{n}$ on the domain boundary, and unit normal vector $\mathbf{n}_s$ on the interface. (b) Interpolation stencil at a domain boundary.

3.1. Equilibrium contact angles

Let us consider an equilibrium of an interface contacting a wall with a prescribed contact angle θ. We take the simulation parameters, $h = 1/128, \epsilon = 0.12\sqrt{h}, \Delta t = 5/128$, and mesh size 256×128 on the computational domain, $\Omega = (0,2) \times (0,1)$. The initial state is taken to be an rectangle, i.e.,

$$c(x,y) = \begin{cases} 1 & \text{if } 0.7 \leqslant x \leqslant 1.3 \text{ and } 0 \leqslant y \leqslant 0.4, \\ -1 & \text{otherwise.} \end{cases}$$

We stop the numerical computations when the discrete l_2-norm [23] of the difference between $(n+1)$th and nth time step solutions becomes less than 10^{-6}. That is $\|c^{n+1} - c^n\| \leqslant 10^{-6}$. Fig. 7a and b show evolutions of interface with prescribed contact angles $\theta = 45°$ and $\theta = 135°$, respectively. The arrow shows the direction of the evolution and the thicker lines are corresponding steady shapes.

Fig. 8 shows interface lengths with contact angles $\theta = 45°$, 60°, 90°, and 135°.

To find a numerical contact angle, we use the following procedure. Given three points (x_1,y_1),(x_2,y_2), and (x_3,y_3) on the interface (see Fig. 9), we calculate the center and the radius of the circle which passes through the three points. We compute the center points x_c and y_c from

$$(x_1 - x_c)^2 + (y_1 - y_c)^2 = (x_2 - x_c)^2 + (y_2 - y_c)^2,$$
$$(x_2 - x_c)^2 + (y_2 - y_c)^2 = (x_3 - x_c)^2 + (y_3 - y_c)^2,$$

and calculate the radius $r = \sqrt{(x_i - x_c)^2 + (y_i - y_c)^2}$. Then the x-intercepts of the circle are $x = x_c \pm \sqrt{r^2 - y_c^2}$ and a derivative at the contact point is

$$\tan\theta = \frac{dy}{dx}\left(x_c + \sqrt{r^2 - y_c^2}, 0\right) = \frac{\sqrt{r^2 - y_c^2}}{y_c}.$$

Finally, we define the numerical contact angle as $\theta = \mathrm{mod}(\tan^{-1}(\sqrt{r^2 - y_c^2}/y_c), \pi)$.

In Fig. 10, the symbols '◇', '△', '∘', and '∗' are the numerical results that we are compared with the analytical values (solid lines) for contact angles with $\theta = 45°$, 60°, 90°, and 135°, respectively. The proposed method is shown to result in a slope of the interface that is consistent with the prescribed contact angle value.

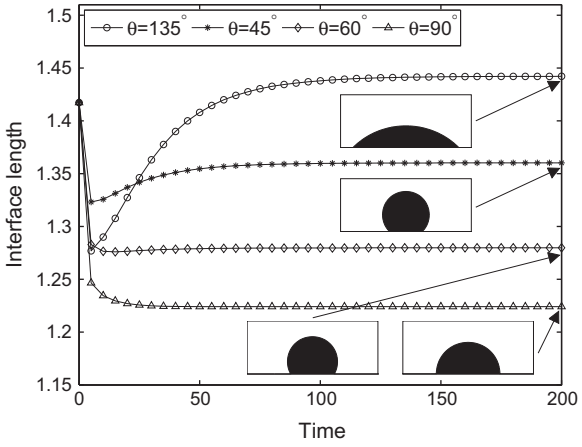

Fig. 8. The interface lengths with contact angles $\theta = 45°$, 60°, 90°, and 135°.

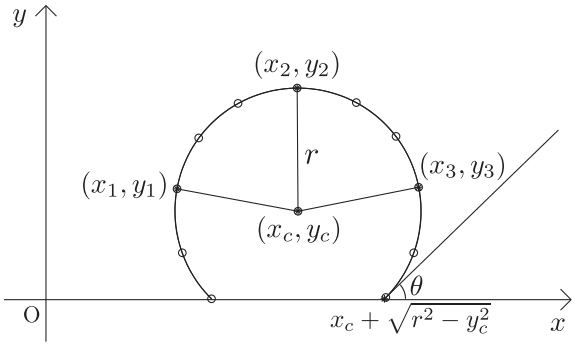

Fig. 9. Definition of numerical contact angle.

The mesh refinement convergence results with various prescribed contact angles are given in Table 1. The results suggest that the numerical contact angles converge to the theoretical contact angle values.

3.2. Small and large contact angles – 20° and 160°

In this section, we test contact angles with below and above 45–135° to demonstrate the accuracy and robustness of the proposed contact angle boundary formulation.

When a contact angle is $\theta = 20°$, the angle is between 18.4349° and 26.5651°, therefore we use $c_{i+2,1}^{n+1}$ and $c_{i+3,1}^{n+1}$ to get $c_{i,0}^{n+1}$ value (see Fig. 11).

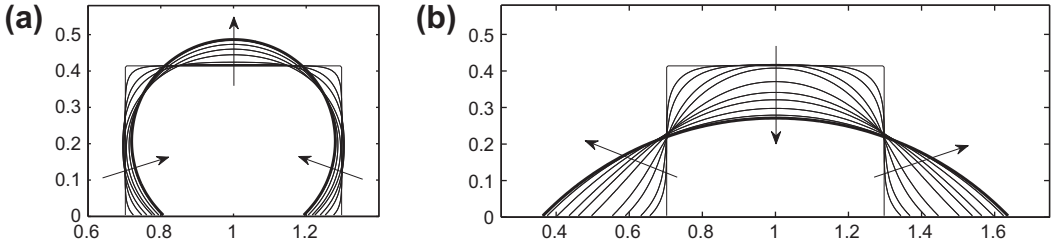

Fig. 7. (a) and (b) are evolutions of interface with prescribed contact angles $\theta = 45°$ and $\theta = 135°$, respectively. The arrow shows the direction of the evolution and the thicker lines are corresponding steady shapes.

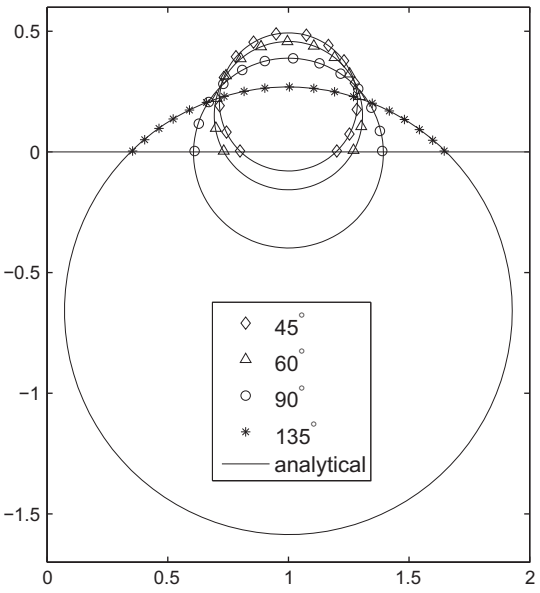

Fig. 10. The symbols '◇', '△', '○', and '∗' are the numerical results that we are compared with the analytical values (solid lines) for contact angles with $\theta = 45°$, 60°, 90°, and 135°, respectively.

$$c_{i,0}^{n+1} = \begin{cases} (1-\alpha)c_{i+2,1}^{n+1} + \alpha c_{i+3,1}^{n+1} & \text{if } c_{i-1,1}^{n+1} > c_{i+1,1}^{n+1}, \\ \alpha c_{i-3,1}^{n+1} + (1-\alpha)c_{i-2,1}^{n+1} & \text{otherwise}, \end{cases}$$

where $\alpha = 1/\tan(20) - 2$. This interpolation is straightforward for a contact angle with $\theta = 160°$.

In case of a contact angle with $\theta = 20°$, the initial state on the computational domain $\Omega = (0,2) \times (0,2)$ is

$$c(x,y) = \begin{cases} 1 & \text{if } 0.25 \leqslant x \leqslant 1.75 \text{ and } 0 \leqslant y \leqslant 1.5, \\ -1 & \text{otherwise}. \end{cases}$$

In case of a contact angle with $\theta = 160°$, the initial state on the computational domain $\Omega = (0,4) \times (0,1)$ is

$$c(x,y) = \begin{cases} 1 & \text{if } 1.7 \leqslant x \leqslant 2.3 \text{ and } 0 \leqslant y \leqslant 0.4, \\ -1 & \text{otherwise}. \end{cases}$$

In both cases, we take the simulation parameters, $h = 1/2^n, \epsilon = 0.28\sqrt{h}$, and $\Delta t = 5h$ for $n = 6$, 7, 8, and 9.

The mesh refinement convergence results are given in Table 2. The results suggest that the numerical contact angles converge to the theoretical contact angle values and the proposed contact angle boundary formulation is accurate and robust.

3.3. Advancing droplet on a solid surface

One way to move a liquid droplet placed on a solid surface is to adjust the gradient of the energetic properties of the surface exposed to the liquid. This can be done by depositing molecular layers or by varying the surface roughness [24]. The computational domain is $\Omega = (0,2) \times (0,1)$ with 256×128 mesh and the initial configuration is a half disk as given in Eq. (16). We took $h = 1/128, \epsilon = 0.17\sqrt{h}$, and $\Delta t = 1/256$.

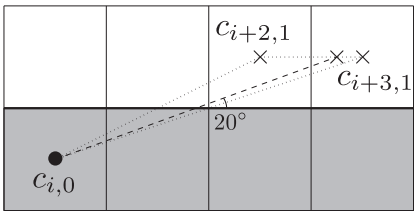

Fig. 11. Characteristic interpolation stencil for the contact angle $\theta = 20°$ at a domain boundary.

$$c(x,y,0) = \tanh\left(\frac{0.25 - \sqrt{(x-1.5)^2 + y^2}}{\sqrt{2}\epsilon}\right). \tag{16}$$

We prescribed the contact angles as $\theta = 135°$ (left contact point) and $\theta = 90°$ (right contact point). After the transition period, the shape of the half disk deforms and reaches a fixed shape. The speed of the contact points converges to a constant value (≈0.05), which is the slope of the line in Fig. 12a.

Fig. 13a shows the distances from the reference position, (1.75,0). '○' and '◇' are the front and back positions, respectively. '∗' is the length of the droplet. In Fig. 13b–e are surface, contour lines, minus gradient, and Laplacian (positive value is solid line and negative value is dotted line) of the chemical potential μ at time $t = 11.7$, respectively. In particular, in Fig. 13d shows the mass flux which directs toward front interface and coming out back interface. Also, it is clear from the Fig. 13e that concentration will increase in the positive area and decrease in the negative region. As a result, the droplet will advance towards the left. This result suggests that we can control the droplet movement on a solid surface by changing contact angles.

3.4. Stability of the scheme

To test an unconditionally gradient stability of the scheme, we perform a numerical experiment with an example of spinodal decomposition of a binary mixture. In the simulations, the initial condition is a random perturbation of the maximum amplitude 0.2 of the uniform state $c = 0$.

$$c(x,y,0) = 0.2\text{rand}(),$$

where the random number, rand( ), is distributed between −1 and 1. A 256×128 mesh is used on the computational domain $\Omega = (0,2) \times (0,1)$ for the spatial discretization and different time step sizes, $\Delta t = 0.1$, 1000, and 100,000 are employed for the time integration. We take the simulation parameters, $h = 1/128$ and $\epsilon = 0.24\sqrt{h}$. The difference between the current scheme and previous unconditionally stable ones is a boundary treatment. In Fig. 14a–c are plots with different time step sizes of $\Delta t = 0.1$, 1000, and 100,000, respectively after 100 time step iterations. The results suggest that the scheme with a contact angle boundary condition indeed unconditionally stable.

Table 1
Convergence results – contact angle with $\theta = 45°$, 60°, 90°, and 135°.

Mesh size	128×64	256×128	512×256	1024×512	Theoretical angle (°)
Numerical angle (°)	40.5210	43.9694	44.2449	44.4974	45
	64.0015	60.8926	60.6834	60.5054	60
	90.9887	90.8424	90.4205	90.1547	90
	136.9205	135.5932	135.2844	135.0116	135

Table 2
Convergence results – contact angle with $\theta = 20^\circ$ and 160°.

Mesh size	128×128	256×256	512×512	1024×1024	Theoretical angle (°)
Numerical angle (°)	12.0235	15.1080	17.3539	19.9366	20
Mesh size	256×64	512×128	1024×256	2048×512	Theoretical angle (°)
Numerical angle (°)	156.9983	157.7652	158.2047	158.2641	160

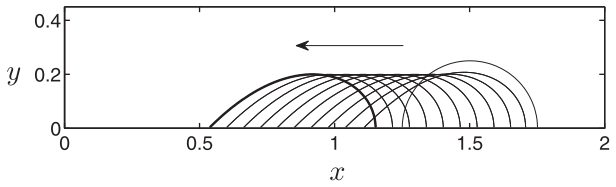

Fig. 12. Snapshots of the moving droplet (from right to left) for $\theta = 135^\circ$ (left contact point) and $\theta = 90^\circ$ (right contact point).

3.5. Drop impact on a solid surface

In this preliminary work, we combine the Navier–Stokes equations to model the two-phase fluid flows contacting a wall. The nondimensional Navier–Stokes equations are

$$\nabla \cdot \mathbf{u} = 0,$$

$$\rho(c)(\mathbf{u}_t + \mathbf{u} \cdot \nabla \mathbf{u}) = -\nabla p + \frac{1}{Re}\nabla \cdot [\eta(c)(\nabla \mathbf{u} + \nabla \mathbf{u}^T)] - \frac{3\sqrt{2}\epsilon}{4We}\nabla \cdot \left(\frac{\nabla c}{|\nabla c|}\right)|\nabla c|\nabla c + \frac{1}{Fr^2}\rho(c)\mathbf{g}.$$

These equations are combined with the advective Cahn–Hilliard equation:

$$c_t + \mathbf{u} \cdot \nabla c = \frac{1}{Pe}\Delta \mu.$$

Here $\mathbf{u}$, p, ρ, η, and $\mathbf{g}$ denote the velocity, pressure, density, viscosity, and gravity, respectively. The dimensionless parameters are Reynolds number, *Re*, Weber number, *We*, Froude number, *Fr*, and Peclet number, *Pe* [22].

In the first experiment, we consider a drop lying on a solid surface surrounded by another liquid. A simulation of this problem has previously been performed by Zahedi et al. using a level-set method [25]. The initial drop is circular with non-dimensional radius $r = 1.0$ centered at $(0, 0.75)$ in non-dimensional computational domain $\Omega = (-3, 3) \times (0, 3)$. The density ratio is $\rho_1/\rho_2 = 1$ (ρ_1 and ρ_2 are the densities inside and outside the drop, respectively) and the initial velocity is zero. To show role of inertia plays, we neglected gravity effects. In this simulation we use the parameters: $\epsilon = 0.014$, $Re = 20$, $We = 0.6$, and $Pe = 0.1/\epsilon$. Mesh size 512×256 and time step $\Delta t = 10^{-4}$ are used. Fig. 15 shows the wetting on the solid wall for nine different snapshots. The snapshots

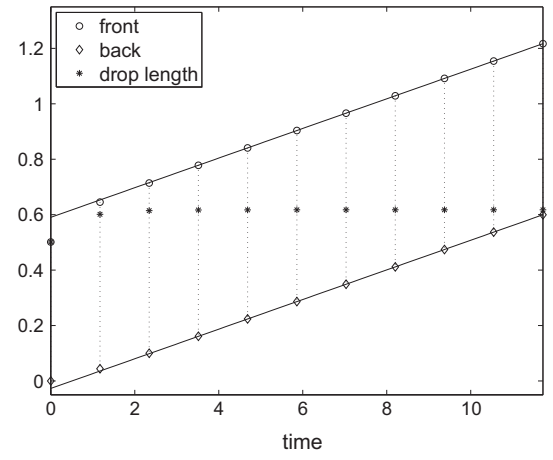

(a)

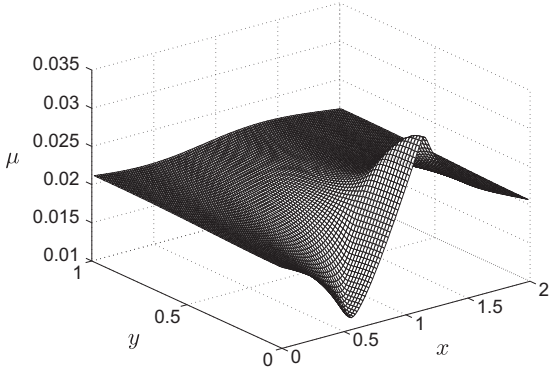

(b) μ surface

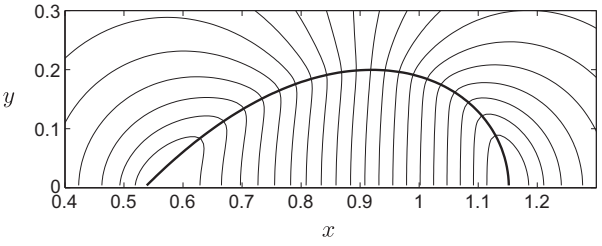

(c) μ contour lines

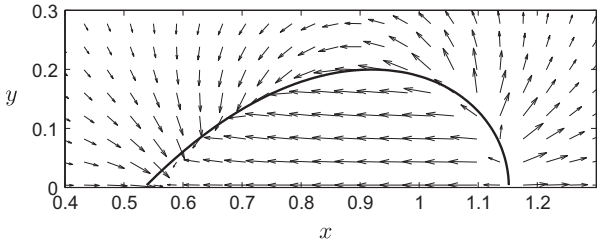

(d) $-\nabla\mu$

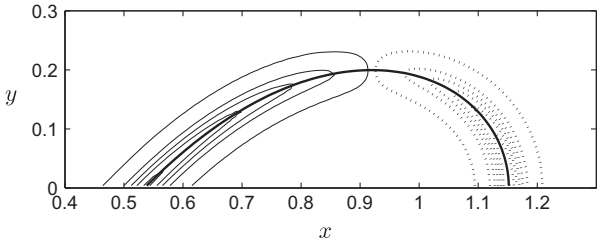

(e) $\Delta\mu$

Fig. 13. (a) The distances from the reference position, *(1.75, 0)*. '$\circ$' and '$\diamond$' are the front and back positions, respectively. '$*$' is the length of the droplet. (b–d), and (e) are surface, contour lines, minus gradient, and Laplacian of the chemical potential μ at time $t = 11.7$, respectively.

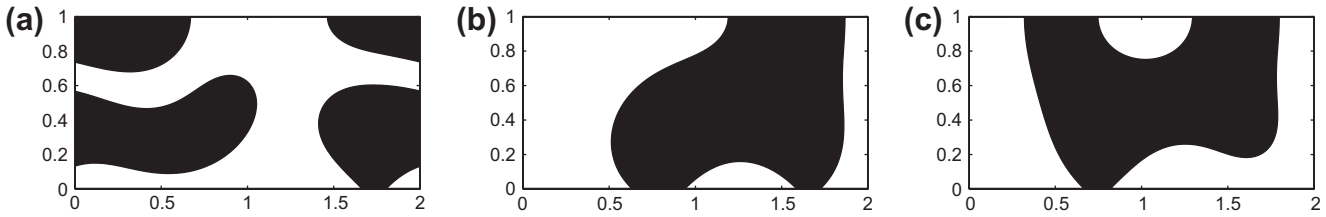

Fig. 14. (a–c) are filled contours at $c = 0$ with different time step sizes of $\Delta t = 0.1$, 1000, and 100,000, respectively.

can be compared with the snapshots from the level-set computation in [25]. Using our proposed contact angle boundary formulation, characteristic interpolation for a contact angle $\theta = 110.02^\circ$ at the wall $y = 0$, we can get the qualitatively similar results. Note that this drop oscillates toward equilibrium due to the resistance of the drop to change its motion.

In the second experiment, we consider the evolution of interfaces with different Bond numbers in order to investigate the gravity effect. The initial drop is circular with non-dimensional radius $r = 1$ centered at $(0,1)$ in non-dimensional computational domain $\Omega = (-2,2) \times (0,4)$. The density ratio is $\rho_1{:}\rho_2 = 10{:}1$ (ρ_1 and ρ_2 are the densities inside and outside the drop, respectively) and the initial velocity is zero. In this simulation we use the parameters: $\epsilon = 0.03$, $Re = 100$, $We = 10$, and $Pe = 200/\epsilon$. Mesh size 256×256 and time step $\Delta t = 2 \times 10^{-4}$ are used. Fig. 16a and b show evolutions of the interface with different Bond numbers $Bo = 1$ and 3, respectively. The results in Fig. 16 show that our results and the previous results of Reznik et al. [26] are in good agreement. And from the result, we can see the followings: (1) the drop spread downwards along the surface by the gravity effect; (2) as the Bond number is increased, the drop is more wetted.

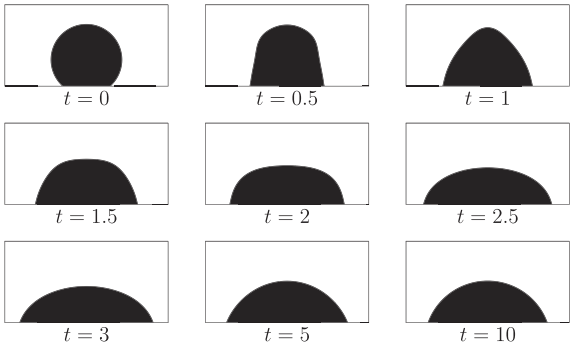

Fig. 15. Wetting of a liquid drop on a solid surface.

4. Conclusions

In this paper, we have proposed a new contact angle boundary formulation for solving the CH equation with a contact angle boundary condition. A key ingredient of the proposed algorithm is based on a characteristic interpolation. We presented various numerical tests showing that the scheme is robust and accurate. The algorithm recovers the prescribed contact angles at the boundary accurately. We implemented it with an unconditionally gradient stable conservative numerical scheme. We demonstrated computationally that the scheme is indeed unconditionally stable.

Acknowledgments

This research was supported by Basic Science Research Program through the National Research Foundation of Korea (NRF) funded by the Ministry of Education, Science and Technology (2008-C00044).

References

[1] Rowlinson JS, Widom B. Molecular theory of capillarity. New York: Dover Publications; 2003.
[2] Young T. An essay on the cohesion of fluids. Philos Trans R Soc London 1805;95:65–87.
[3] Manservisi S, Scardovelli R. A variational approach to the contact angle dynamics of spreading droplets. Comput Fluids 2009;38:406–24.
[4] Cahn JW. On spinodal decomposition. Acta Metall Mater 1961;9:795–801.
[5] Cahn JW, Hilliard JE. Free energy of a nonuniform system. I. Interfacial free energy. J Chem Phys 1958;28:258–67.
[6] Ding H, Spelt PDM. Wetting condition in diffuse interface simulations of contact line motion. Phys Rev E 2007;75. 046708-1–8.
[7] Jacqmin D. Contact-line dynamics of a diffuse fluid interface. J Fluid Mech 2000;402:57–88.

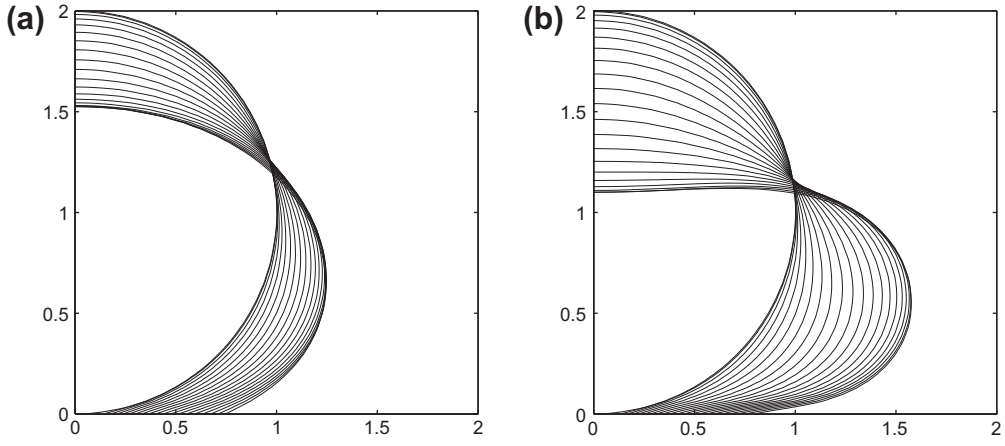

Fig. 16. The gravity effect. Evolutions of the interface with (a) $Bo = 1$ and (b) $Bo = 3$.

[8] Khatavkar VV, Anderson PD, Duineveld PC, Meijer HHE. Diffuse interface modeling of droplet impact on a pre-patterned solid surface. Macromol Rapid Commun 2005;26:298–303.
[9] Khatavkar VV, Anderson PD, Meijer HHE. Capillary spreading of a droplet in the partially wetting regime using a diffuse-interface model. J Fluid Mech 2007;572:367–87.
[10] Menech MD. Modeling of droplet breakup in a microfluidic T-shaped junction with a phase-field model. Phys Rev E 2006;73. 031505-1–9.
[11] Takada N, Matsumoto J, Matsumoto S, Ichikawa N. Application of a phase-field method to the numerical analysis of motions of a two-phase fluid with high density ratio on a solid surface. J Comput Sci Technol 2008;2:318–29.
[12] Villanueva W, Amberg G. Some generic capillary-driven flows. Int J Multiphase Flow 2006;32:1072–86.
[13] Villanueva W, Sjödahl J, Stjernström M, Roeraade J, Amberg G. Microdroplet deposition under a liquid medium. Langmuir 2007;23:1171–7.
[14] Furihata D. A stable and conservative finite difference scheme for the Cahn–Hilliard equation. Numer Math 2001;87:675–99.
[15] Kay D, Welford R. A multigrid finite element solver for the Cahn–Hilliard equation. J Comput Phys 2006;212:288–304.
[16] Kim J, Kang K, Lowengrub J. Conservative multigrid methods for Cahn–Hilliard fluids. J Comput Phys 2004;193:511–43.
[17] Miranville A, Zelik S. Exponential attractors for the Cahn–Hilliard equation with dynamic boundary conditions. Math Methods Appl Sci 2005;28:709–35.
[18] Carlson A, Do-Quang M, Amberg G. Modeling of dynamic wetting far from equilibrium. Phys Fluids 2009;21. 121701-1–4.
[19] Eyre DJ. <http://www.math.utah.edu/~eyre/research/methods/stable.ps>.
[20] Eyre DJ. Computational and mathematical models of microstructural evolution. In: Warrendale, PA: The Material Research Society; 1998.
[21] Kim J, Bae H-O. An unconditionally stable adaptive mesh refinement for Cahn–Hilliard equation. J Korean Phys Soc 2008;53:672–9.
[22] Kim J. A continuous surface tension force formulation for diffuse-interface models. J Comput Phys 2005;204:784–804.
[23] Choi J-W, Lee HG, Jeong D, Kim J. An unconditionally gradient stable numerical method for solving the Allen–Cahn equation. Phys A 2009;88:1791–803.
[24] Tabeling P. Introduction to microfluidics. New York: Oxford University Press; 2005.
[25] Zahedi S, Gustavsson K, Kreiss G. A conservative level set method for contact line dynamics. J Comput Phys 2009;228:6361–75.
[26] Reznik SN, Yarin AL. Spreading of a viscous drop due to gravity and capillarity on a horizontal or an inclined dry wall. Phys Fluids 2002;14:118–32.